



Structural phase transition and multiferric properties of Y, Eu co-doped $\text{BiFe}_{0.97}\text{Mn}_{0.03}\text{O}_3$ nanoparticles

Zhiyong Ge¹, Jiangwei Zhu², Hongtao Xue¹, and Weiwei Mao^{1,*}

¹ Jiangsu Provincial Engineering Research Center of Low Dimensional Physics and New Energy & School of Science, Nanjing University of Posts and Telecommunications, Nanjing 210023, China

² Co-Innovation Center for Sustainable Forestry in Southern China, Nanjing Forestry University, Nanjing 210037, China

Received: 16 September 2023

Accepted: 15 December 2023

Published online:
28 December 2023

© The Author(s), under exclusive licence to Springer Science+Business Media, LLC, part of Springer Nature, 2023

ABSTRACT

Pure BiFeO_3 (BFO), $\text{BiFe}_{0.97}\text{Mn}_{0.03}\text{O}_3$ and $\text{Bi}_{0.9}\text{Y}_x\text{Eu}_{0.1-x}\text{Fe}_{0.97}\text{Mn}_{0.03}\text{O}_3$ ($x = 0.03, 0.05$ and 0.07) nanoparticles were synthesized to study the relation between multiferric properties and structure. The XRD results in such undoped and doped samples suggested that the rhombohedral structure was distorted due to the co-doping, whereas the modification has an impact on the structural parameters. Scanning electron microscopy studies clearly showed the decrease of average grain size due to the co-doping of Y and Eu in the BFO. Moreover, the presence of Y and Eu caused an increment in the magnetic and ferroelectric properties, and the sample with the highest M_r (0.154 emu/g) and H_c (9.02 kOe) values was the $x = 0.07$ one. The origin of such enhanced multiferric properties has been demonstrated on the structural phase transition.

1 Introduction

At ambient temperature, BiFeO_3 (BFO) is the only single-phase multiferric material exhibiting both ferroelectric and antiferromagnetic characteristics. In the disciplines of spintronics, magnetoelectric and photoelectric sensors, BFO can be used due to its high ferroelectric Curie temperature and high antiferromagnetic Neel temperature [1–5]. Although BFO has high remanent polarization strength in theory, bismuth element of BFO is easy to volatilize and part of Fe^{3+} changes to Fe^{2+} during the preparation process, resulting in more oxygen vacancies, which makes it difficult to prepare a sample with high remanent polarization. In addition, the magnetic properties make materials a promising candidate for various kind of applications such as magnetic

resonance imaging, magnetic storage devices and catalysts [6, 7]. But the helical magnetic structure of bismuth ferrite makes the magnetic moment locked and can not exhibit larger magnetic properties, so the practical application is limited [8, 9]. Doping rare earths ions (Eu [10], Er [11], La and Pr [12], etc.) at the A-site or transition metal (Co [13], Mn [14], etc.) at the B-site have tried to improve the ferroelectric and ferromagnetic ordering in pure BFO. For example, La^{3+} and Bi^{3+} ions have approximate radii of 1.032 and 1.030, respectively, and it is effective to stabilize the BFO structure with a small replacement of bismuth ion at the A-site by lanthanum ion [15]. Furthermore, it is effective way to reduce the leakage current and enhance magnetization of BFO by c-doping rare earths ions and transition metal ions at the A-site and the B-site, respectively [16–19]. In

Address correspondence to E-mail: maoww@njupt.edu.cn

addition, some researches have been done to control the structure distortion by substituting with rare earth ions in BFO, in order to decrease the leakage current and improve the magnetic characteristics [20–22]. BFO doped by europium ion is reported to have good ferromagnetic characteristics and a strong coercive field [23, 24]. Eu-doping can lead to a rhombohedral-to-cubic phase transformation (R3c to Pm-3 m) and 10% Eu-doping can induce dramatically 50% phase transformation [25]. In comparison, Y doping only can induce less phase transformation. Very recently, Shi et al. reported the existence of a bridging phase in rare earth doped BFO compounds. The net magnetization of the sample will be considerably larger if the weak ferromagnetism in the rhombohedral phase released from the spiral spin structure [26]. Therefore, our present work aims to explore the influence of phase transformation on multiferroic properties by Eu, Y and Mn co-substitution in BFO. In order to obtain pure nanomaterials, alternative methods such as hydrothermal, solid-state reaction, and sol-gel methods are used [27, 28]. The sol-gel route have been used in this work, because it is the most popular way to prepare nanosized BFO due to its simplicity, low cost, and good control over the structure and properties.

This work reports on the synthesis of $\text{Bi}_{0.9}\text{Y}_x\text{Eu}_{0.1-x}\text{Fe}_{0.97}\text{Mn}_{0.03}\text{O}_3$ ($x = 0.03, 0.05$ and 0.07) nanoparticles prepared by sol-gel method. We have investigated the effect of phase transition on multiferroic properties of bismuth ferrite. Different doping ratios were designed to control the degree of phase transition, and the existence of appropriate cubic phase (Pm-3 m) could enlarge the magnetic and ferroelectric properties. These findings demonstrate the immense potential of BFO with the suitable doping of Y, Eu, and Mn in multifunctional applications.

2 Materials and methods

BFO, $\text{BiFe}_{0.97}\text{Mn}_{0.03}\text{O}_3$ (M3) and $\text{Bi}_{0.9}\text{Y}_x\text{Eu}_{0.1-x}\text{Fe}_{0.97}\text{Mn}_{0.03}\text{O}_3$ (BYEFMO) ($x = 0.03, 0.05$ and 0.07 , named Y3E7M5, Y5E5M5 and Y7E3M3, respectively) nanoparticles were prepared by a sol-gel route. All the reagents in this work are presented in Table 1. To create the precursor solutions, the stoichiometric amounts of high purity Yttrium oxide, europium oxide, bismuth oxide, manganese oxide, iron nitrate powders were gradually dissolved in 15 ml of nitric acid (65%). The solution was magnetically stirred until a clear solution was obtained. Slowly add distilled water into the clear solution, stirring as you add. As a chelating agent, tartaric acid was added to the precursor solution along with the equal quantity of total metallic ions. The solution was heated at 90°C to a hot plate magnetic stirring at 400 rpm until the solution was changed into the gel. The resulting gel was then dried at 70°C for 48 h, prebaked for 2 h at 250°C , and finally annealed in the air for 2 h at 550°C .

3 Results and discussion

Figure 1 shows X-ray diffraction (XRD) patterns of pure BFO, M3 and BYEFMO nanoparticles. The primary peaks of the pure BFO are shown in Fig. 1a to be associated with a rhombohedral structure with the standard crystal data of the JCPDS Card (71-2494). For the doped samples, no characteristic peaks of Yttrium oxide, Europium oxide or Manganese Oxide can be observed, which suggests that the ions were successfully incorporated into the lattice. With Y, Eu co-doping, the XRD peaks shift to higher 2θ values to show the mild lattice distortion. For the doped samples, the doublet peaks corresponding to the (104) and (110) planes around 32° shift to higher angle and nearly merged into a single peak. The lattice parameters of

Table 1 Reagents in this work

Chemical formula	Molecular weight	Amount to use			
		x = 0	x = 0.03	x = 0.05	x = 0.07
Bi_2O_3	465.96	2.0968	2.0968	2.0968	2.0968
$\text{Fe}(\text{NO}_3)_3 \cdot 9\text{H}_2\text{O}$	404.00	3.9188	3.9188	3.9188	3.9188
Y_2O_3	225.81	0	0.0339	0.0565	0.0790
Eu_2O_3	351.93	0.1760	0.1232	0.0880	0.0528
MnO	70.94	0.0212	0.0212	0.0212	0.0212

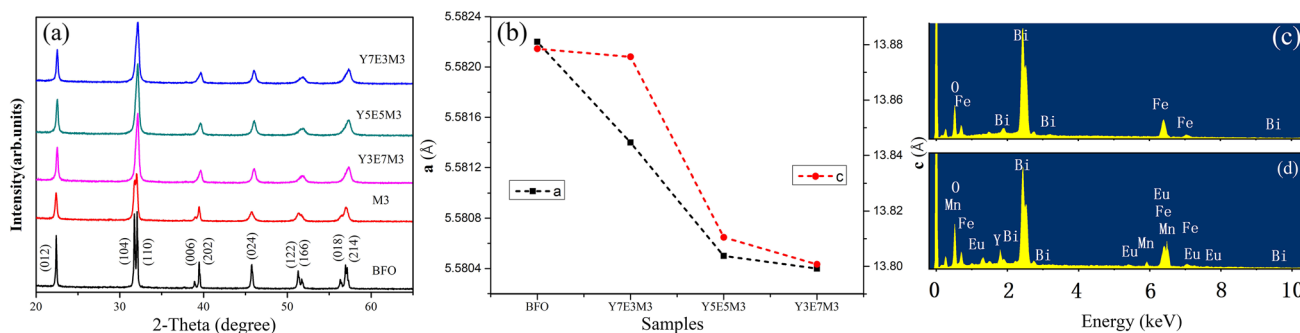


Fig. 1 **a** XRD of pure BFO, M3 and BYEFMO nanoparticles. **b** the crystal structure parameters of the samples obtained from XRD patterns. EDX patterns of **c** BFO and **d** Y5E5M3

the prepared samples were estimated based on the XRD data and the results are presented in Table 2. Additionally, Table 2 provides a comparison of the lattice parameters obtained from XRD patterns. It can be observed that the values of the lattice parameters obtained in this research closely align with the literature values. The contraction of the unit cell, or the reduction in lattice parameters brought on by the replacement of the larger Bi³⁺ (1.17 Å) ions with the smaller Eu³⁺ (1.07 Å) and Y³⁺ (0.9 Å) dopants. Figure 1b displays the (a, c) parameters variation versus samples. The lattice parameters a and c of pure BFO are biggest of all the samples, which is attributed to the ionic radius of Bi is bigger than the ionic radius of Eu and Y. Furthermore, the lattice parameters a and c decreases with the increase of Eu dopant content. This is because of the dopant Eu³⁺ (1.07 Å) with bigger ionic radii than Y³⁺ (0.9 Å). The similar results were also observed in other studies, such as: Y and transition metal ions codoped BFO [18]; Eu and La codoped BFO [31]; Er doped BFO [11]. The elemental analysis was carried out using the energy dispersive X-ray spectroscopy (EDX) analysis. Typical EDX patterns of BFO

and Y5E5M3 have been shown in Fig. 1c and d. The chemical composition of BFO agrees with the nominal one 1:1:3 approximately. Besides the obvious signals for O, Bi, and Fe, the EDX spectra show weak signal of Y, Eu and Mn. The measured quantitative values demonstrate the atomic percentage of 16.89% Bi, 1.18% Y, 1.31% Eu, 18.12% Fe, 0.87% Mn for Y5E5M3, respectively. It can be seen from the above results that Y, Eu and Mn ions are effectively incorporated into the matrix material.

In order to clarify the phase structure and ratio, the XRD of all samples was investigated by Rietveld refinement method using Fullprof suite software. Figure 2 displays the Rietveld refinement outcomes of the BFO and BYEFMO samples. Pure BFO crystal structures are rhombohedra with space group (R3c), whereas BYEFMO crystal structures are characterized as rhombohedral and cubic (Pm-3 m) phase. Table S1 (as shown in Supplementary Materials) provides the fitting parameters of BYEFMO samples. The calculated bond length distance of Fe–O bonds in the doped BFO samples is smaller than those in the undoped BFO samples, which suggests that doping makes some

Table 2 The crystal structure parameters of the samples in this work and other similar works

Sample	a (Å)	c (Å)	Volume (Å ³)	References
BFO	5.5822	13.8785	374.523	This work
Y7E3M3	5.5814	13.8756	374.337	This work
Y5E5M3	5.5805	13.8105	372.865	This work
Y3E7M3	5.5804	13.8007	372.670	This work
BFO	5.580	13.871	373.965	[29]
Bi _{0.99} Y _{0.01} Fe _{0.98} Ni _{0.02} O ₃	5.575	13.857	373.084	[29]
Bi _{0.95} Ho _{0.05} FeO ₃	5.574	13.810	371.611	[22]
Bi _{0.90} Ho _{0.10} FeO ₃	5.564	13.664	366.437	[22]
BFO	5.5805	13.8731	374.1492	[30]
Bi _{0.90} Eu _{0.10} FeO ₃	5.5712	13.8319	371.7961	[30]

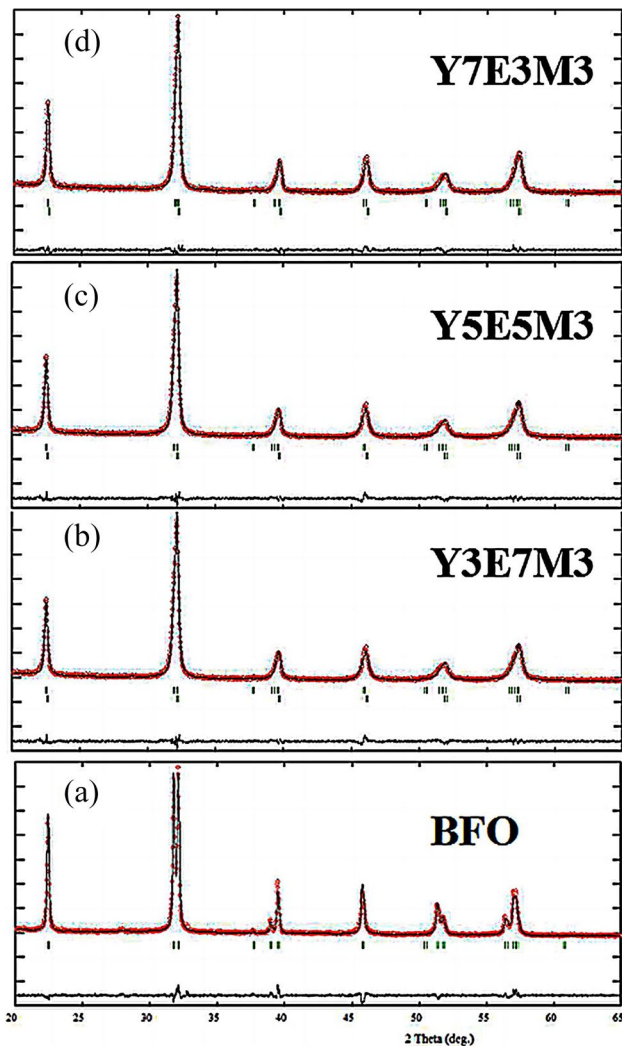


Fig. 2 a–d The Rietveld refinement results of as-prepared BFO, Y3E7M5, Y5E5M5 and Y7E3M3 samples. The discrepancies between the calculated and observed spectra are displayed in a bottom-up graphic. Ticks represent Bragg reflections

impact on the magnetic moment in the Fe^{3+} position. Meanwhile, as the rise in the value of x , the Pm-3m phase decreases. Thus we comment that Eu ions mainly contribute to the conversion of the rhombohedral phase (R3c) to the cubic phase (Pm-3m). Additionally, the Fe–O–Fe bond angles decrease with the x increases. This might contribute to an increase in net macroscopic magnetism for the Y3E7M5, Y5E5M5 and Y7E3M3 samples.

Figure 3 displays the SEM photographs of BFO and BYEFMO samples. It can be clearly seen from Fig. 3 that the crystallization of the four samples is good. The grain size is uneven, and there is obvious

agglomeration. For the pure sample, the grains are irregular elliptical stone-like. There are certain pores between the crystal grains, and the grain size is about 160 nm. As can be seen from Fig. 3b, d, with the introduction of doping ions, the morphology of the sample basically does not change significantly, and the crystal grains are still irregular. The elliptical stone shape, the agglomeration phenomenon is still the same, but the grain size has been reduced and its grain size has been reduced from the original 100–200 nm to about 50–100 nm. The size and morphology of the three doped samples are similar. In order to observe the morphology and size of the samples clearly, TEM measurement has been presented in Fig. S1 and Fig S2 (as shown in Supplementary Materials). The TEM results are consistent with the SEM results. The reduction in grain size caused by doping may be related to oxygen vacancies. Bi^{3+} volatilizes to form a small amount of oxygen vacancies in the BFO. The volatilization of Bi^{3+} can be reduced by doping, inhibiting the generation of oxygen vacancies in the sample. The reduction of vacancies will slow down the movement of oxygen ions during the sintering process, reduce the growth rate of grains, and reduce the grain size [32]. In addition, doping inhibits the grain growth that can be attributed to the lattice contraction derived from the replacement of smaller ionic radius, which is consistent with the outcome of XRD parameters.

The polarization hysteresis (P - E) loops were recorded with an applied electric field (E) of 20 kV/cm in order to investigate the ferroelectric behavior of all the samples. The results are depicted in Fig. 4. All of the samples demonstrate unsaturated P - E loops, giving clear indication of the ferroelectric behavior but in a lossy loop. The leakage current can be linked to the harmful features of these samples, such as defect or oxygen vacancies. The Y7E3M3 sample exhibits the best ferroelectric hysteresis loop of all the samples with a remnant polarization (P_r) of $0.562 \mu\text{C}/\text{cm}^2$ and a coercive electric field (E_c) of 10.92 kV/cm under the applied electric field of 20 kV/cm. While for Y3E7M3 and Y5E5M3 samples, the remnant polarization decreased because of the increased leakage current and the lower resistivity. According to the J - E curves (Fig. 5), Y and Eu doping can minimize the leakage current density of BFO and hence improve ferroelectric property [33, 34].

The leakage current density as a function of the applied electric field is displayed in Fig. 5 for measurements made at room temperature. Obviously, the

Fig. 3 SEM photographs of pure BFO (a), Y3E7M5 (b), Y5E5M5 (c) and Y7E3M3 (d) nanoparticles

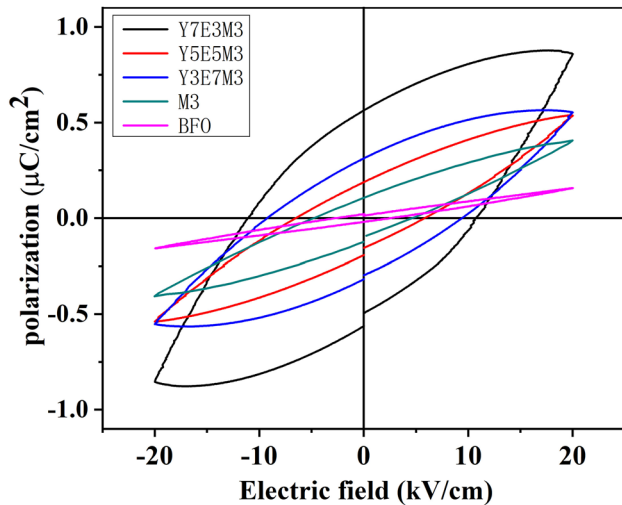
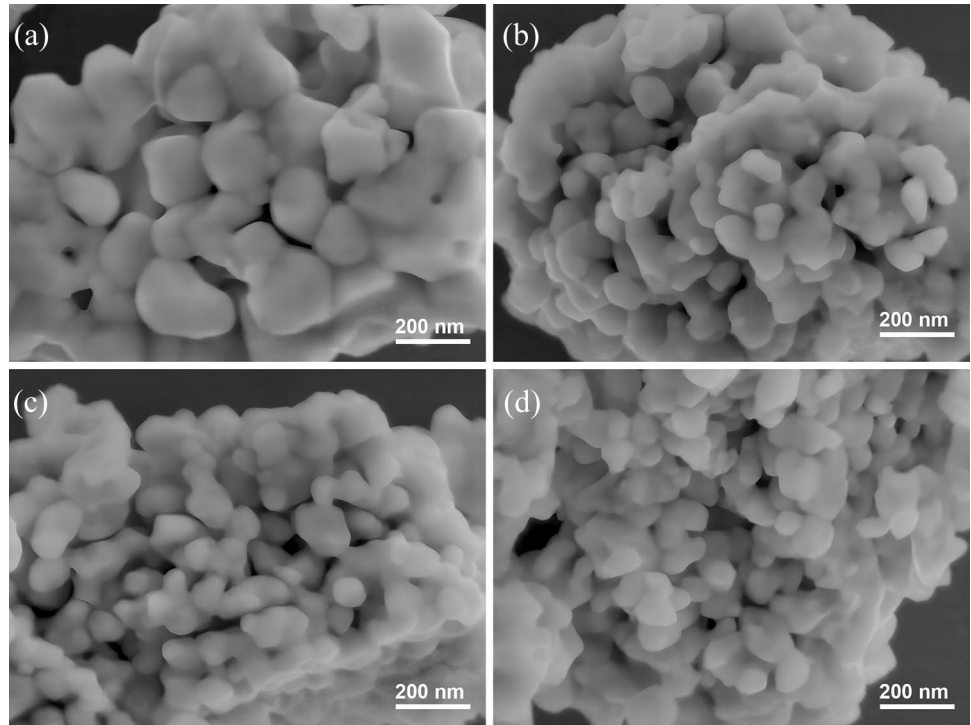


Fig. 4 Polarization hysteresis loops for all the samples measured at room temperature

leakage current density of all the samples increases rapidly with the increase of external electric field, especially under strong electric field. The leakage current density of the BYEFMO nanoparticles were much lower than that of pure BFO. Under maximum applied electric field of 20 kV/cm, the current densities are $1.0932 \times 10^{-3} \text{ A/cm}^2$, $4.5068 \times 10^{-5} \text{ A/cm}^2$ for

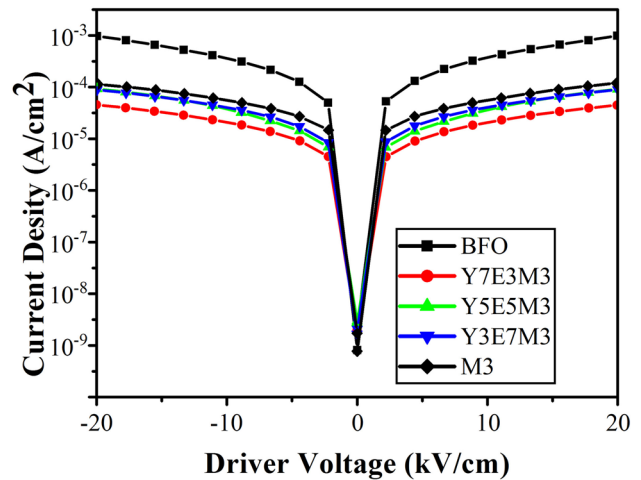


Fig. 5 Leakage current density as a function of electrical field for pure BFO, M3 and BYEFMO nanoparticles at room temperature

undoped BFO and Y7E3M3 sample, respectively. At all applied electric fields, the measured value of the leakage current density for the Y7E3M3 sample reduces by nearly two orders of magnitude when compared to the pure BFO.

The main magnetic parameters, namely saturation magnetization, remanent magnetization, coercivity can

be extracted from the hysteresis loops [35, 36]. Figure 6 shows the magnetic hysteresis (M - H) curves for Mn doped and Mn, Eu and Y co-doped BFO nanoparticles. A nearly linear M - H loop with a tiny remnant magnetization is found for undoped BFO, which is compatible with the cycloidal spin structure. The M - H loops eventually transform into normal hysteresis loops with improved remnant magnetization as x grows, which is a property of the weakly ferromagnetic antiferromagnets. Compared with the pure BFO, magnetic properties of BYEFMO are effectively enhanced with the increase of Y doping concentration. Domain pattern can be obtained from the M - H loops. When there is no external magnetic field, the magnetization vector bit directions within the magnetic domain are disordered, and the macroscopic appearance is non-magnetic. As the external magnetic field increases, domain wall displacement and magnetization vector rotation occur successively, which is the initial magnetization process. When the external magnetic field is removed, the magnetic domains do not return to their original state, thus exhibiting residual magnetization. When a reverse magnetic field is applied, the magnetic domains will cancel each other out with the applied reverse magnetic field intensity, resulting in hysteresis. More importantly, the highest values of remnant magnetization (M_r) (~ 0.154 emu/g) and coercive field

(H_c) (~ 9.02 kOe) were obtained in Y7E3M3 sample. Jadav et al. synthesized Gd doped BFO using modified sol gel technique [37]. The magnetic curves are not saturated in magnetic field of about 15,000 Gauss. Compared with pure BFO, Gd doped sample shows enhanced ferromagnetic property M_r and M_{max} about 0.00056 emu/g and 0.00577 emu/g, respectively. Kebede et al. studied the impact of Sm doping in BFO nanoparticles on its ferromagnetic effect [38]. The obtained M_r and H_c were around 0.12 emu/g and 1.062 kOe for $\text{Bi}_{0.90}\text{Sm}_{0.10}\text{FeO}_3$, 0.11 emu/g and 0.805 kOe for $\text{Bi}_{0.85}\text{Sm}_{0.15}\text{FeO}_3$, respectively. Abdelmadjid et al. investigated the magnetic properties of Pb and Ti co-doped BFO multiferroic ceramics [39]. The measured values of M_r increase with the addition of Ti from 0.007 emu/g ($\text{Bi}_{0.9}\text{Pb}_{0.1}\text{Fe}_{0.95}\text{Ti}_{0.05}\text{O}_3$) to 0.020 emu/g ($\text{Bi}_{0.9}\text{Pb}_{0.1}\text{Fe}_{0.80}\text{Ti}_{0.20}\text{O}_3$). The coercivity decreases monotonically with the doing of Ti from 0.204 kOe ($\text{Bi}_{0.9}\text{Pb}_{0.1}\text{Fe}_{0.95}\text{Ti}_{0.05}\text{O}_3$) down to 0.104 kOe ($\text{Bi}_{0.9}\text{Pb}_{0.1}\text{Fe}_{0.80}\text{Ti}_{0.20}\text{O}_3$). Khomchenko et al. reported that the M_r was about 0.043 emu/g for the Sr and Mn co-doped BFO ceramic obtained by a solid-state reaction [40]. Kar et al. synthesized the polycrystalline $0.56\text{Bi}_{1-x}\text{La}_x\text{FeO}_3-0.44\text{BaTiO}_3$ ceramics through the conventional solid-state reaction process [41]. The measured remnant magnetizations (M_r) for $x = 0.20$ La doped sample are 0.0983 emu/g and 0.158 emu/g

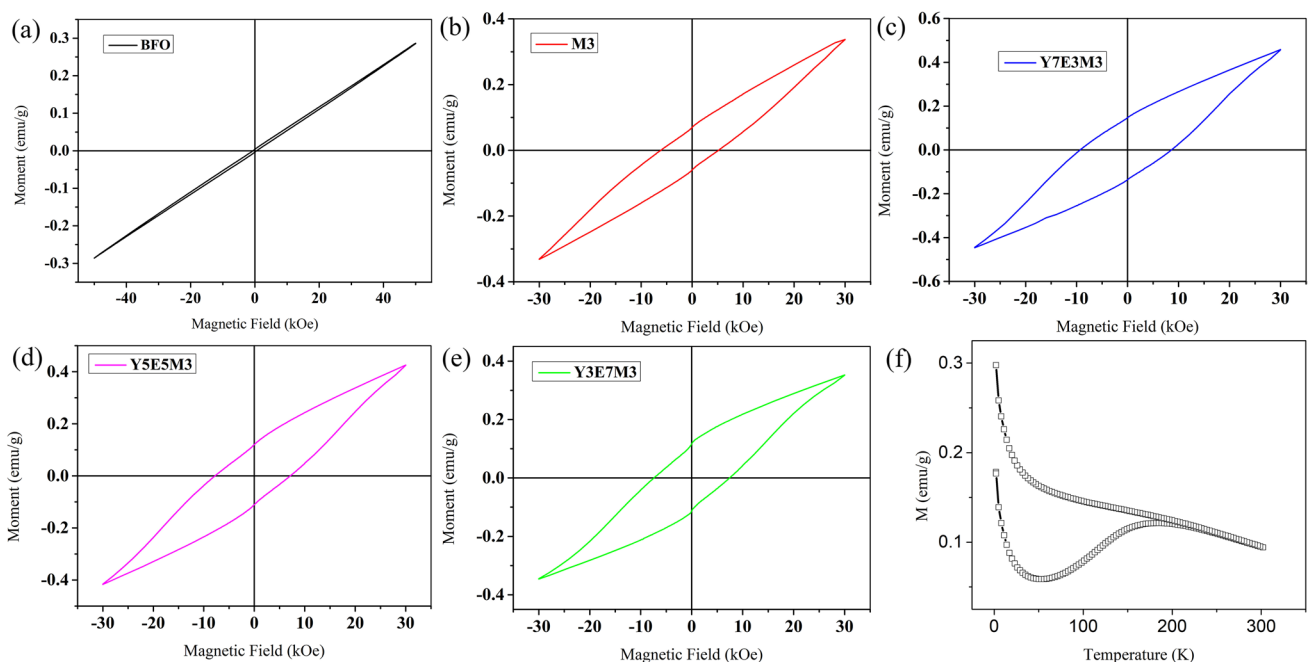


Fig. 6 a The magnetic hysteresis (M - H) curves for (a) pure BFO, b M3, c Y7E3M3, d Y5E5M3, e Y3E7M3, f the zero-field cooled and field cooled magnetization vs. temperature plots for Y7E3M3

at room temperature and 5 K, respectively, which are significantly greater than the pure one. Apparently, the values in the present work are well comparable with those previous values.

Clearly, the ferromagnetic property can greatly improved by doping Mn into pure BFO, and after Y, Eu co-doping ferromagnetic property can be further enhanced. It is important to note that Y, Eu co-doping into BFO can boost macroscopic magnetization by prohibiting the cycloidal spin structure and relieving the weak ferromagnetism, because the co-doping can reduce the grain size and result in domain size getting similar as the period length of the spin cycloid (~ 62 nm) [42]. The change of the magnetization maybe result from the structural evolution from rhombohedral phase (R3c) to cubic phase (Pm-3 m). BFO exhibits weak ferromagnetism at room temperature due to a magnetic cycloidal spin structure. The net magnetization will actually be larger if the weak ferromagnetism of the R3c phase is released from the spiral spin structure. The R3c phase and the Pm-3 m phase are both clearly weakly ferromagnetic, but the weak ferromagnetism in the R3c phase is substantially stronger than that in the Pm-3 m phase. [43, 44]. Thus the ratio of R3c phase to Pm-3 m phase plays a key role in the change of the magnetization. Analyzing from the Rietveld refinement results, both the less the ratio of R3c phase to Pm-3 m phase and the smaller Fe–O–Fe bond angles could give strong evidence of the highest ferromagnetic property occurred in $x = 0.07$. The change in magnetization may be more significantly influenced by structural evolution. Figure 6f shows the ZFC (zero-field cooling) and FC (field cooling) magnetization curves of Y7E3M3 sample, which is measured between 2 and 300 K at 1kOe. The clear difference between ZFC and FC curves with the blocking temperature about 220 K. This split is similar to that found for ferromagnetic and ferrimagnetic materials, suggesting that Y7E3M3 becomes ferro/ferrimagnetic property [17, 45].

4 Conclusion

In summary, we conduct a comparison analysis on the pure BFO, $\text{BiFe}_{0.97}\text{Mn}_{0.03}\text{O}_3$ and $\text{Bi}_{0.9}\text{Y}_x\text{Eu}_{0.1-x}\text{Fe}_{0.97}\text{Mn}_{0.03}\text{O}_3$ ($x = 0.03, 0.05$ and 0.07) nanoparticles. XRD revealed that Y, Eu co-doping-induced crystal structural transformation from

the rhombohedral phase (R3c) to the cubic phase (Pm-3 m). Meanwhile, crystal structural transformation plays an indispensable role in improving the ferroelectric polarization and releasing the locked magnetization. Hence, our present work may provide a platform to adjust the ferroelectric and ferromagnetic properties with the suitable doping of Y, Eu, and Mn. Compared to other materials, the simultaneous enhancement of magnetic and ferroelectric properties suggests the potential application in multiferroic devices, multifunctional sensors and high-density memory devices.

Author contributions

ZG: Investigation, Formal analysis, Writing—original draft preparation, Methodology, Software. JZ: Data collection. HX: Methodology, Software, Data curation. WM: Discussion, Writing—review&editing, Project administration, Resources.

Funding

We acknowledge the National Natural Science Foundation of China (61874060, 61911530220, U1932159).

Data availability

The datasets generated and analyzed during the current study are available on reasonable request.

Declarations

Conflict of interest The authors declare that they have no known competing financial interests or personal relationships that could have appeared to influence the work reported in this paper.

Research involving human participants and/or animals This article does not contain any studies with human participants or animals performed by any of the authors.

Informed consent Informed consent was obtained from all individual participants included in the study.

Supplementary Information The online version contains supplementary material available at <https://doi.org/10.1007/s10854-023-11824-6>.

References

- N.A. Spaldin, M. Fiebig, *Science*. **309**, 391–392 (2005)
- W. Amdouni, M. Fricaudet, M. Otoničar, V. Garcia, S. Fusil, J. Kreisel, H. Maghraoui-Meherzi, B. Dkhil, *Adv. Mater.* **35**, 2301841 (2023)
- S. Matzen, S. Gable, N. Lequet, S. Yousfi, K. Rani, T. Maroutian, G. Agnus, H. Bouyanfif, P. Lecoeur, *Appl. Phys. Lett.* **121**, 142901 (2022)
- Y. Wang, C. Guo, M. Chen, Y. Liang, H. Han, H. Chen, Y. Lin, D. Yi, H. Huang, C.-W. Nan, J. Ma, *Adv. Funct. Mater.* **33**, 2213787 (2023)
- A. Haykal, J. Fischer, W. Akhtar, J.Y. Chauleau, D. Sando, A. Finco, F. Godel, Y.A. Birkhölzer, C. Carrétéro, N. Jaouen, M. Bibes, M. Viret, S. Fusil, V. Jacques, V. Garcia, *Nat. Commun.* **11**, 1704 (2020)
- T. Dippong, I.G. Deac, O. Cadar, E.A. Levei, *Nanomaterials* **11**, 2232 (2021)
- T. Dippong, E.-A. Levei, D. Toloman, L. Barbu-Tudoran, O. Cadar, *J. Anal. Appl. Pyrol.* **158**, 105281 (2021)
- A. Cardona Rodríguez, A. Reiber, I.K. Schuller, D. Muraca, J. Gabriel, Ramírez, *J. Magn. Magn. Mater.* **563**, 169917 (2022)
- R. Safi, H. Shokrollahi, *Prog. Solid State Chem.* **40**, 6–15 (2012)
- Z. Jiang, A. Peng, M. Liu, G. Liu, G. Zhang, *Mod. Phys. Lett. B* **33**, 1950094 (2019)
- S. Sharma, J.M. Siqueiros, O.R. Herrera, *J. Alloys Compd.* **853**, 156979 (2021)
- C.E. Camayo, S. Gaona, J.C.F.V. Raigoza, *J. Magn. Magn. Mater.* **527**, 167733 (2021)
- Y. Wang, X. Zhang, *J. Magn. Magn. Mater.* **560**, 169570 (2022)
- X. Zhang, X. Yang, Z. Wang, Q. Pan, B. Chu, R. Zuo, *J. Mater. Sci.* **33**, 15520–15532 (2022)
- Q. Zhang, X. Zhu, Y. Xu, H. Gao, Y. Xiao, D. Liang, J. Zhu, J. Zhu, D. Xiao, *J. Alloys Compd.* **546**, 57–62 (2013)
- M. Tefera Kebede, S. Devi, V. Dillu, S. Chauhan, *Mater. Sci. Eng.* **283**, 115859 (2022)
- P.J. Jose, U. Rathod, C. Savaliya, S. Jethva, A. Panchasara, S. Katba, M. Keshvani, M. Vagadia, A. Ravalvia, *J. Electron. Mater.* **51**, 6689–6698 (2022)
- Y. Lin, Q. Jiang, H. Deng, *J. Solid State Chem.* **303**, 122450 (2021)
- S. Godara, N. Sinha, B. Kumar, *Ceram. Int.* **42**, 1782–1790 (2016)
- P. Suresh, P.D. Babu, S. Srinath, *J. Appl. Phys.* **115**, 17D905 (2014)
- W.W. Mao, X.F. Wang, Y.M. Han, X.A. Li, Y.T. Li, Y.F. Wang, Y.W. Ma, X.M. Feng, T. Yang, J.P. Yang, W. Huang, *J. Alloys Compd.* **584**, 520–523 (2014)
- M. Kumar, H. Pandey, *J. Supercond. Novel Magn.* **36**, 1269–1276 (2023)
- Z. Hu, M. Li, J. Liu, L. Pei, J. Wang, B. Yu, X. Zhao, *J. Am. Ceram. Soc.* **93**, 2743–2747 (2010)
- J. Liu, L. Fang, F. Zheng, S. Ju, M. Shen, *Appl. Phys. Lett.* **95**, 022511 (2009)
- Y. Zhu, C. Quan, Y. Ma, Q. Wang, W. Mao, X. Wang, J. Zhang, Y. Min, J. Yang, X. Li, W. Huang, *Mater. Sci. Semiconduct. Process.* **57**, 178–184 (2017)
- X.X. Shi, X.Q. Liu, X.M. Chen, *Adv. Funct. Mater.* **27**, 1604037 (2017)
- T. Dippong, E. Andrea Levei, O. Cadar, I. Grigore Deac, M. Lazar, G. Borodi, I. Petean, *J. Alloys Compd.* **849**, 156695 (2020)
- T. Dippong, E.A. Levei, O. Cadar, *Int. J. Mol. Sci.* **23**, 8483 (2022)
- P. Banerjee, A. Franco, R.Z. Xiao, *Mater. Today* **46**, 4716–4719 (2021)
- A.L. Zinnatullin, I.Y. Nosov, M.A. Cherosov, A.G. Kiiamov, F.G. Vagizov, *J. Solid State Chem.* **312**, 123216 (2022)
- A. Kaiyum, M.A. Hossain, M. Sarowar Hossain, R. Rashid, A. Kumar, M.A. Hakim, M.N.I. Khan, *J. Magn. Magn. Mater.* **560**, 169350 (2022)
- J. Liu, L. Wang, M. Niu, R. Jiang, Y. Liu, D. Xu, C. Jin, *J. Magn. Magn. Mater.* **527**, 167777 (2021)
- T. Wang, T. Xu, S. Gao, S.H. Song, *Ceram. Int.* **43**, 4489–4495 (2017)
- X. Zhang, Y. Sui, X. Wang, Y. Wang, Z. Wang, *J. Alloys Compd.* **507**, 157–161 (2010)
- T. Dippong, E.A. Levei, I.G. Deac, I. Petean, O. Cadar, *Int. J. Mol. Sci.* **23**, 3097 (2022)
- T. Dippong, E.A. Levei, C. Leostean, O. Cadar, *J. Alloys Compd.* **868**, 159203 (2021)
- G.D. Jadav, S.K. Chavda, P.V. Kanjariya, J.A. Bhalodia, *Mater. Today* **47**, 510–516 (2021)
- M.T. Kebede, V. Dillu, S. Devi, S. Chauhan, *Physica B* **624**, 413374 (2022)
- K. Abdelmadjid, V.A. Lukacs, F. Gheorghiu, *Ceram. Int.* **49**, 32711–32718 (2023)
- V.A. Khomchenko, M. Das, M.S.C. Henriques, J.A. Paixão, *J. Magn. Magn. Mater.* **585**, 171142 (2023)

41. B.S. Kar, M.N. Goswami, P.C. Jana, J. Alloys Compd. **861**, 157960 (2021)
42. T.-J. Park, G.C. Papaefthymiou, A.J. Viescas, A.R. Moodenbaugh, S.S. Wong, Nano Lett. **7**, 766–772 (2007)
43. H. Dai, Z. Chen, R. Xue, T. Li, H. Liu, Y. Wang, Appl. Phys. A **111**, 907–912 (2013)
44. T. Elbakraoui, E.B. Benamar, A. Ouasri, A. El-Bey, M. Taibi, A. Belayachi, A. Dinia, M. Abd-Lefdil, J. Solid State Chem. **325**, 124178 (2023)
45. P. Suresh, B.K. Hazra, B.R. Kumar, T. Chakraborty, P.D. Babu, S. Srinath, J. Alloys Compd. **863**, 158719 (2021)

Publisher's Note Springer Nature remains neutral with regard to jurisdictional claims in published maps and institutional affiliations.

Springer Nature or its licensor (e.g. a society or other partner) holds exclusive rights to this article under a publishing agreement with the author(s) or other rightsholder(s); author self-archiving of the accepted manuscript version of this article is solely governed by the terms of such publishing agreement and applicable law.